Efficient CuO/Ag₂WO₄ photoelectrodes for photoelectrochemical water splitting using solar visible radiation

E. Mustafa, [ID] *[a] E. A. Dawi, [ID] [b] Z. H. Ibupoto, [ID] [c] A. M. M. Ibrahim, [ID] [d] A. Elsukova, [ID] [e]
X. Liu, [ID] [a] A. Tahira, [ID] [f] R. E. Adam, [ID] [a] M. Willander [ID] [a] and O. Nur [ID] [a]

Water splitting energy production relies heavily on the development of high-performance photoelectrochemical cells (PECs). Among the most highly regarded semiconductor materials, cupric oxide (CuO) is an excellent photocathode material. Pristine CuO does not perform well as a photocathode due to its tendency to recombine electrons and holes rapidly. Photocathodes with high efficiency can be produced by developing CuO-based composite systems. The aim of our research is to develop an Ag₂WO₄/CuO composite by incorporating silver tungstate (Ag₂WO₄) nanoparticles onto hydrothermally grown CuO nanoleaves (NLs) by successive ionic layer adsorption and reaction (SILAR). To prepare CuO/Ag₂WO₄ composites, SILAR was used in conjunction with different Ag₂WO₄ nanoparticle deposition cycles. Physicochemical characterization reveals well-defined nanoleaves morphologies with tailored surface compositions. Composite CuO/Ag₂WO₄ crystal structures are governed by the monoclinic phase of CuO and the hexagonal phase of Ag₂WO₄. It has been demonstrated that the CuO/Ag₂WO₄ composite has outstanding performance in the PEC water splitting process when used with five cycles. In the CuO/Ag₂WO₄ photocathode, water splitting activity is observed at low overpotential and high photocurrent density, indicating that the reaction takes place at low energy barriers. Several factors contribute to PEC performance in composites. These factors include the high density of surface active sites, the high charge separation rate, the presence of favourable surface defects, and the synergy of CuO and Ag₂WO₄ photoreaction. By using SILAR, silver tungstate can be deposited onto semiconducting materials with strong visible absorption, enabling the development of energy-efficient photocathodes.

1 Introduction

The production of hydrogen from solar-powered water splitting has the potential to significantly strengthen renewable energy reservoirs. This is because it has a high density, clean energy carrier, abundant solar energy, and a low energy barrier.[1–4] The phenomenon of water splitting is caused by two parallel reactions, namely the oxygen evolution reaction (OER) and the hydrogen evolution reaction (HER), which exhibit different kinetics in terms of activation energy. Particularly, the OER

ᵃDepartment of Sciences and Technology, Linköping University, Campus Norrköping, SE-601 74 Norrköping, Sweden. E-mail: elfatih.mohammed.mustafa@liu.se; elfatihmustafa@gmail.com

ᵇNonlinear Dynamics Research Centre (NDRC), Ajman University, P. O. Box 346, United Arab Emirates

ᶜInstitute of Chemistry, University of Sindh, 76080, Jamshoro, Pakistan

ᵈDepartment of Pharmaceutical Chemistry, Jazan University, P. O. Box 346, Kingdom of Saudi Arabia

ᵉDepartment of Physics, Chemistry and Biology, Linköping University, SE-58183 Linköping, Sweden

ᶠInstitute of Chemistry, Shah Abdul Latif University Khairpur Mirs, 66020, Sindh, Pakistan

process is an energy-intensive reaction, which limits the overall efficiency of water splitting. This is the reason we have limited the portion of hydrogen production from water splitting to date.[5,6] In view of the high energy requirement for water splitting, photoelectrochemical (PEC) water splitting is a versatile technology that is characterized by a low energy demand owing to its use of photons, and it allows the separation of two reactions easily, namely OER and HER.[7–11]

The choice of materials for fabricating photocathodes is based on their ability to absorb strong bands in the visible region, while also being low in cost, earth abundant, cost-effective, and environmentally friendly. There are a variety of semiconducting materials available, including n-type materials like TiO₂, WO₃, ZnO, Fe₂O₃, and BiVO₄,[12–16] as well as p-type materials like p-Si, Cu₂O, CuO, p-InP, and p-CdS[17–23] that have been examined for use as photoanodes and photocathodes for solar water electrolysis, respectively. Among these metal oxides, cupric oxide (CuO) is an exemplary photocathode material with many interesting features like narrow bandgap (1.3–1.7 eV), low cost, earth abundant, and easy to prepare by environment friendly methods.[19,24–28] In addition to gas sensing, photocatalysis, lithium-ion batteries, and solar cells, CuO has been

studied extensively for a wide range of applications.[29–32] A further advantage of CuO is its high visible light absorption band, which makes it highly suitable for PEC water splitting.[33–36] Due to the fast charge carrier recombination rate, CuO has relatively low photoactivity towards HER.[11,36,37] To overcome the recombination rate, different techniques are utilized to amend the chemical composition and surface characteristics of CuO like reducing particle size and fabricating composite materials.[38,39] There have been a variety of methods used to synthesize CuO nanostructures with various morphologies,[40] among which CuO nanoleaves (NLs) grown by hydrothermal method is simple, inexpensive, scale up, and eco-friendly.[27,40] In addition, silver-based semiconductors are considered suitable materials for increasing PEC water splitting efficiency.[41,42] In recent years, the deposition of silver tungsten oxide or silver tungstate (Ag_2WO_4) nanoparticles by using a successive ionic layer adsorption and reaction (SILAR) method with various cycles onto metal oxide semiconductors with improved performance has been reported.[43–47] The SILAR method allows controlling the thickness of the deposition based on solution concentration and cycle number up to micrometers.[48] First, hydrothermal method was used to deposit nanoleaves of CuO. Low-cost, simple, scalable, eco-friendly, and environmentally friendly are some of the advantages of the hydrothermal method. The SILAR method was used due to the fact that it is a well-controlled method for producing uniform growth layers for the development of hybrid materials, as well as a cost effective method and requires little growth time. Based on these considerations, we used both of these methods in order to demonstrate photoelectrochemical water splitting using hybrid materials.

CuO/Ag_2WO_4 composites offer rapid charge transfer at the electrode–electrolyte interface by preventing electron and hole recombination charges. They also possess a tunable surface with a high density of active sites, resulting from various metallic oxidation states of Cu, Ag, and W, as well as unique oxygen surface defects, which enables advanced PEC water splitting. Composites of CuO with Ag_2WO_4 can also be used to demonstrate the effective transfer of charges at the interface. To our knowledge, no research has been conducted on the CuO/Ag_2WO_4 composite prepared by hydrothermal and SILAR methods in order to assess its performance in the PEC water splitting process.

Using hydrothermal and SILAR methods, we investigated the deposition of Ag_2WO_4 nanoparticles onto CuO NLs. Composites of CuO and Ag_2WO_4 have been studied using a variety of deposition cycles, including 5, 10, and 15, and its response to water splitting activity has been investigated. The CuO/Ag_2WO_4 composite has been examined by structural and photoelectrochemical characterization.

2 Experimental section

2.1. Synthesis of CuO/Ag_2WO_4 photoelectrodes

CuO/Ag_2WO_4 composites were synthesized in two steps, as schematically illustrated in Fig. 1.

Initially, fluorine-doped tin oxide (FTO) glasses (thickness 2.3 mm, surface resistivity ~7 Ω sq^{-1} and transmittance 80–82% (visible)) were spun coated with CuO seed solution, then annealed at 120 °C for 1 minute. To prepare a seed solution, 0.01 M of copper(II) acetate monohydrate $Cu(C_2H_3O_2)_2 \cdot H_2O$ was dissolved in 99% methanol at 60 °C with stirring. Later, a solution of 0.03 M of potassium hydroxide (KOH) in 99% methanol was slowly added drop by drop to the copper(II) acetate solution that was also being stirred at 60 °C. Copper precursors were prepared by mixing copper(II) nitrate hemi(pentahydrate) $(CuN_2O_6 \cdot 2.5H_2O)$ 0.05 M in 100 mL of deionized water with hexamethylenetetramine (HMT) 0.025 M. Upon preparation, a seed layer of CuO was applied through spin coating to FTO glass substrates. Substrates were then soaked in CuO solution before being baked at 80–85 °C for 5–6 hours. As a result of the growth process, a black CuO product was deposited on FTO glass substrates, indicating that CuO nanostructures were successfully formed. Additionally, using the SILAR method,
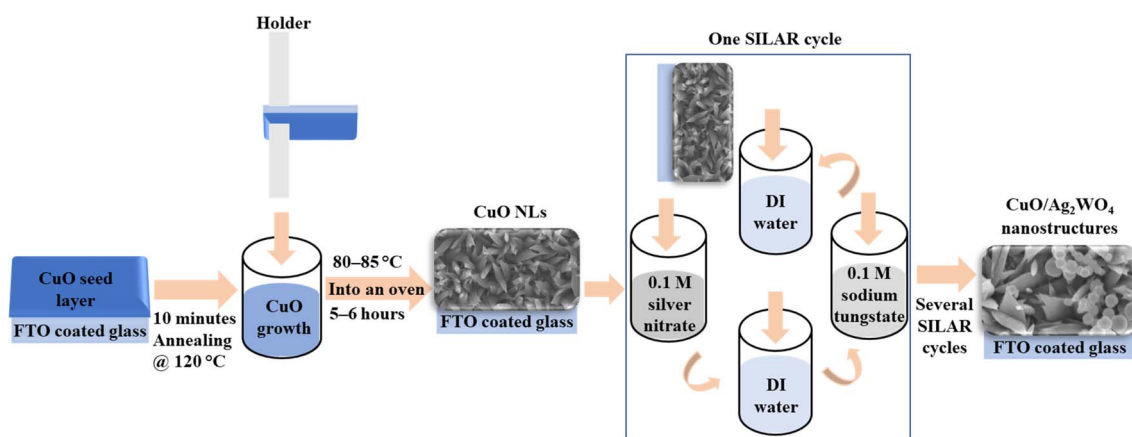

Fig. 1 Schematic diagram showing the synthesis process of the CuO/Ag_2WO_4 composites. Preparation of CuO seed solution by drop-wise addition of 0.03 M potassium hydroxide (KOH) in 99% methanol to 0.01 M of copper(II) acetate monohydrate $Cu(C_2H_3O_2)_2 \cdot H_2O$ in 99% methanol at 60 °C with stirring. For CuO growth, 0.05 M copper(II) nitrate hemi(pentahydrate) $(CuN_2O_6 \cdot 2.5H_2O)$ in 100 mL of deionized water was mixed with 0.025 M hexamethylenetetramine (HMT). The deposition of silver tungstate (Ag_2WO_4) nanoparticles (NPs) onto CuO nanoleaves (NLs) was achieved using the successive ionic layer adsorption and reaction (SILAR) method with different cycles.

silver tungstate was deposited on CuO in order to prepare composites of CuO and Ag_2WO_4. As part of this experiment, CuO photoelectrodes were immersed for two minutes in 0.1 M silver nitrate ($AgNO_3$) solution to adsorb enough silver ions (Ag^+), and the excess ions were then removed by submerging them in deionized (DI) water for two minutes. A second step consisted of dipping the photoelectrodes into 0.1 M sodium tungstate ($Na_2WO_4 \cdot 2H_2O$) solution for 2 minutes, and then transferring them to a DI water bath for two minutes. This dipping process is called a SILAR cycle, and the deposition of silver tungstate was performed for 5 and 10 SILAR cycles to prepare optimum Ag_2WO_4 nanoparticles. A final step was to improve the adhesion of Ag_2WO_4 by placing the photoelectrodes in an electric oven at 60 °C for 3 hours.

2.2. Structure, chemical composition, and morphology characterizations

We examined the morphology of fabricated photoelectrodes with a FE-SEM (Gemini 500, Zeiss) equipped with a 10 kV field emission gun. XRD was used to determine the phase identification of these samples on a Panalytical X'pert diffractometer with Cu K(α) ($\lambda = 1.54$ Å) 45 kV and 40 mA. We used a Linköping double Cs corrected FEI Titan3 60–300, operated at 300 kV, to perform high angle annular dark field scanning transmission electron microscopy (HAADF-STEM) imaging and EDX spectroscopy characterization. Lacey-carbon Cu TEM grids were utilized to deposit particles obtained by scratching off the sample surface. XPS with Scienta ESCA 200 and a monochromatic Al K(a) source (1486.6 eV) was employed to determine

the chemical composition of CuO/Ag_2WO_4 composites. CasaXPS software was used to analyze the data. Following this, UV-VIS spectroscopy equipment (PerkinElmer Lambda 900 system) was used to analyze the optical properties of samples.

2.3. Photoelectrochemical measurements of CuO/Ag_2WO_4 composite

A three electrode PEC cell with a SP-200 potentiostat (Bio-Logic, Claix, France) was used to investigate the photoelectrochemical properties of the photoelectrodes. PEC cells consist of silver/silver chloride (Ag/AgCl) electrodes in 3 M KCl (reference electrode), platinum wires (counter electrodes), and fabricated electrodes (working electrodes) in 1.0 M sodium hydroxide (NaOH) as electrolyte. It was estimated that the electrode dipped in the electrolyte had an active area of 1 cm^2. Experimental light illumination was performed using a solar simulator (LCS-100, AM 1.5G, 100 W ozone free xenon lamp). Electrochemical impedance spectroscopy (EIS) experiments were conducted at onset potentials of 0.1 V, amplitudes of 0.01 V, and sweeping frequencies of 100 kHz–1 Hz. Quantitative information about the active surface area was estimated by cyclic voltammetry.

3 Results and discussion

3.1. Structural characterization analysis of CuO/Ag_2WO_4 composite

In this study, FE-SEM was employed to investigate the morphology of the CuO NLs, as well as various composites of CuO/Ag_2WO_4 grown on FTO glass substrates. As can be seen in
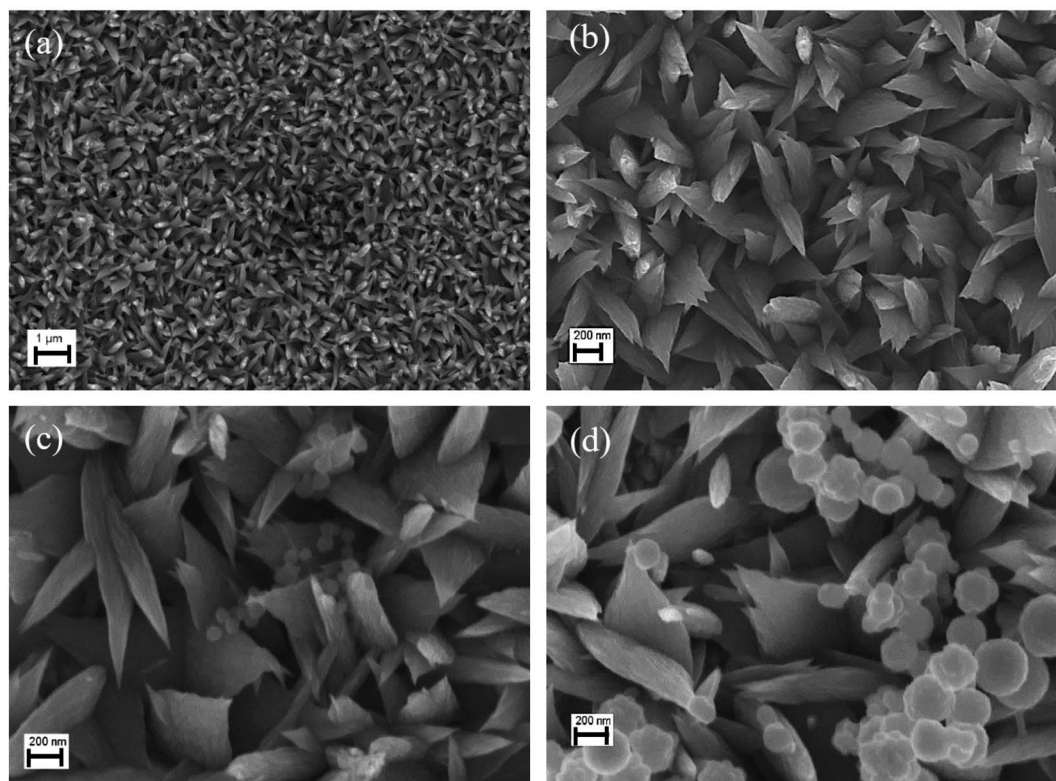

Fig. 2 SEM images of (a), (b) pristine CuO NLs, (c) CuO/Ag_2WO_4 (5 SILAR cycles) and (d) CuO/Ag_2WO_4 (10 SILAR cycles).

Fig. 2(a), the CuO photoelectrode clearly has a very dense morphology and high substrate coverage and uniformity. Using a high magnification SEM image of the CuO photoelectrode, Fig. 2(b) reveals that the nanostructures resemble nano-leaves (300–600 nm). It is confirmed from Fig. 2(c) that Ag_2WO_4 nanoparticles have been deposited on CuO NLs. Using a larger number of SILAR cycles, as demonstrated in Fig. 2(c) and (d), Ag_2WO_4 nanoparticles deposited on CuO NLs grew larger, both in size and agglomeration.

EDX is shown in Fig. 3(a) and elemental mapping is shown in Fig. 3(b), confirming that Ag_2WO_4 nanoparticles were deposited onto CuO NLs. Chemical analysis reveals that the composites mainly consist of Cu, O, Ag, and W atoms. It can be seen from Fig. 3(a) and (b) that fluorine (F) and tin (Sn) elements arose as a result of the chemical composition of FTO glass substrate. The XRD patterns of pristine CuO NLs and various composites of CuO/Ag_2WO_4 deposited on FTO glass substrates are displayed in Fig. 3(c). These results confirm that all reflection peaks of pristine CuO NLs are exactly the same as those exhibited by the monoclinic phase of CuO (see JCPDS no. 96-900-8962) and the tetragonal phase of fluorine doped tin oxide (FTO). Further, after the deposition of Ag_2WO_4 onto the CuO NLs, some additional diffraction patterns were observed that were assigned to the hexagonal phase of Ag_2WO_4 (JCPDs no. 96-900-8962). In contrast to pristine CuO NLs, there is a slight shift of CuO NLs peaks in CuO/Ag_2WO_4 composites. This is due to morphology and size effects. Moreover, the crystallite size of synthesized samples was calculated using the Scherrer equation:[49]
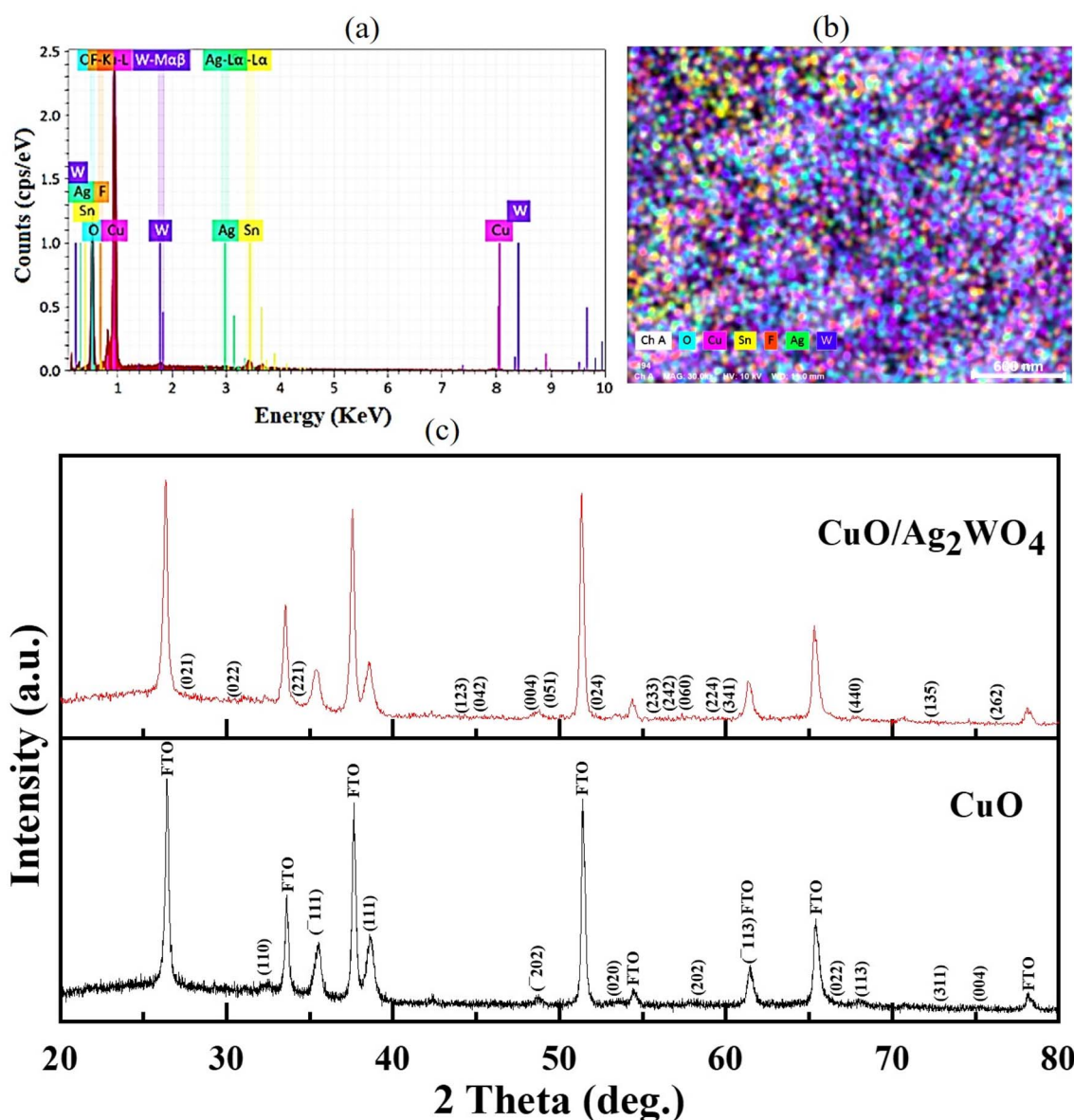
$$D = \frac{k\lambda}{\beta_{hkl} \cos \theta}$$

Fig. 3   (a) EDX of the CuO/Ag_2WO_4 composites, (b) EDX mapping of the CuO/Ag_2WO_4 composites, and (c) XRD patterns of CuO NLs and CuO/Ag_2WO_4 composites.
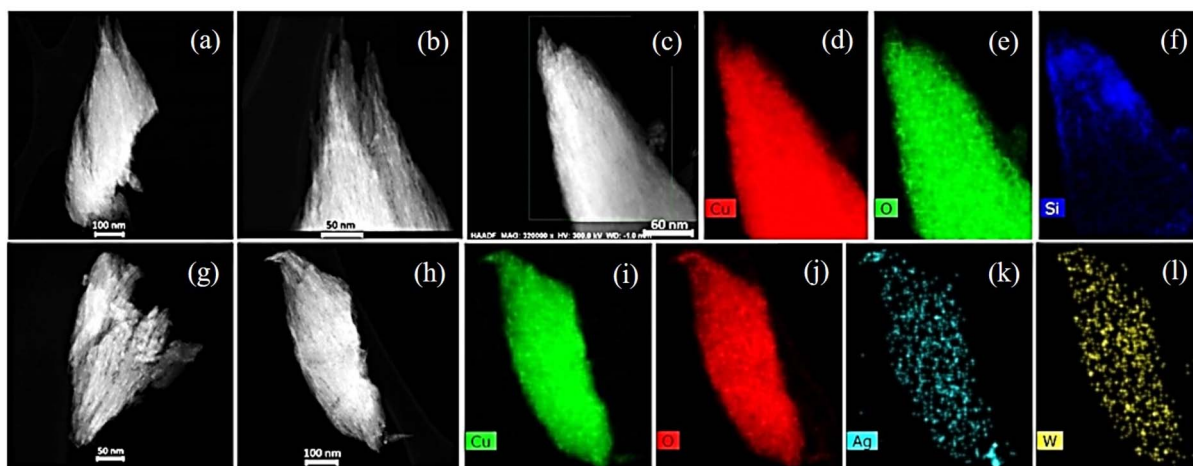

Fig. 4 (a and b) HAADF-STEM images of CuO NLs. (c–f) HAADF-STEM image with corresponding EDX Cu, O and Si elemental maps. (g) HAADF-STEM image of CuO/Ag$_2$WO$_4$ particle. (h–l) HAADF-STEM image of the CuO/Ag$_2$WO$_4$ composites with corresponding Cu, O, Ag, and W elemental maps.

where D is the crystallite size, λ is the X-ray wavelength, θ is the Bragg diffraction angle, β_{hkl} is the full width at half maximum, and k is the Scherrer constant equal to 0.94. The average crystallite size of CuO NLs was found to decreased from 21 to 19 nm after deposition of Ag$_2$WO$_4$ nanoparticles.

Furthermore, HAADF-STEM imaging of CuO particles (Fig. 4(a and b)) revealed that they contain crystalline fibrous filament structures. Particles were found to contain copper and oxygen as indicated by EDX spectra and maps (Fig. 4(c–e)). In some particles presence of Si was observed (Fig. 4(f)). Similar morphologies can be seen in CuO/Ag$_2$WO$_4$ (Fig. 4(g)). The EDX maps in Fig. 4(h–l) show an even distribution of copper, oxygen, silver, and tungsten.

As shown in Fig. 5(a), UV-VIS spectroscopy was used to investigate the optical properties of pristine CuO NLs and CuO/Ag$_2$WO$_4$ composites. CuO/Ag$_2$WO$_4$ composites showed higher light absorption than pristine CuO NLs, which can help to improve HER efficiency. The optical bandgap (E_g) of pure CuO

NLs was measured to be 1.47 eV, while for the CuO/Ag$_2$WO$_4$ composite, it was approximately 1.56 eV (Fig. 5(b)). It was found that Ag$_2$WO$_4$ did not alter CuO's optical bandgap during deposition. Therefore, the CuO/Ag$_2$W$_4$ composite showed a bandgap of 1.56 eV, while pure CuO showed a bandgap of 1.47 eV. As reported in the literature, optical bandgap values range from 1.44 to 1.89 eV.[50,51] The estimated bandgaps are optimal for the absorption of visible solar light, and they are also more conducive to splitting PEC water.

Furthermore, XPS analysis was carried out to understand the surface chemical features of various composites of CuO/Ag$_2$WO$_4$ as shown in Fig. 6. A wide scan spectrum of pristine CuO NLs and CuO/Ag$_2$WO$_4$ composites are shown in Fig. 6. The major peaks in CuO/Ag$_2$WO$_4$ composites inferred to Cu 2p, O 1s, Ag 3d, C 1s (284 eV), Cu 3s (122.5 eV), Cu 3p (76 eV) and W 4f revealing the perfect chemical composition as described by EDX. Fig. 7(a) displays high-resolution spectrum of Cu 2p. The main peaks can be assigned to Cu 2p$_{3/2}$ (933.65 eV) and Cu 2p$_{1/2}$
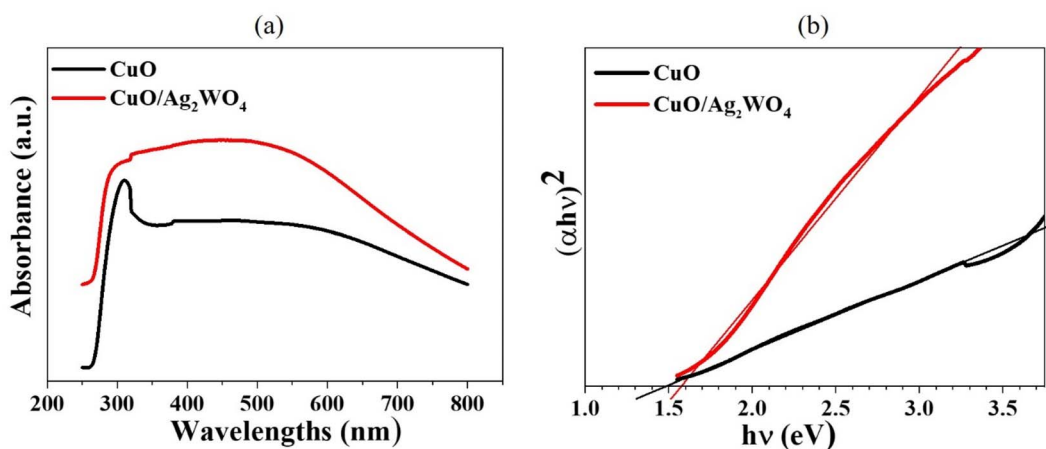

Fig. 5 (a) The optical absorbance of the CuO and the CuO/Ag$_2$WO$_4$ composites, and (b) the plots of $(\alpha h\nu)^2$ versus $h\nu$.
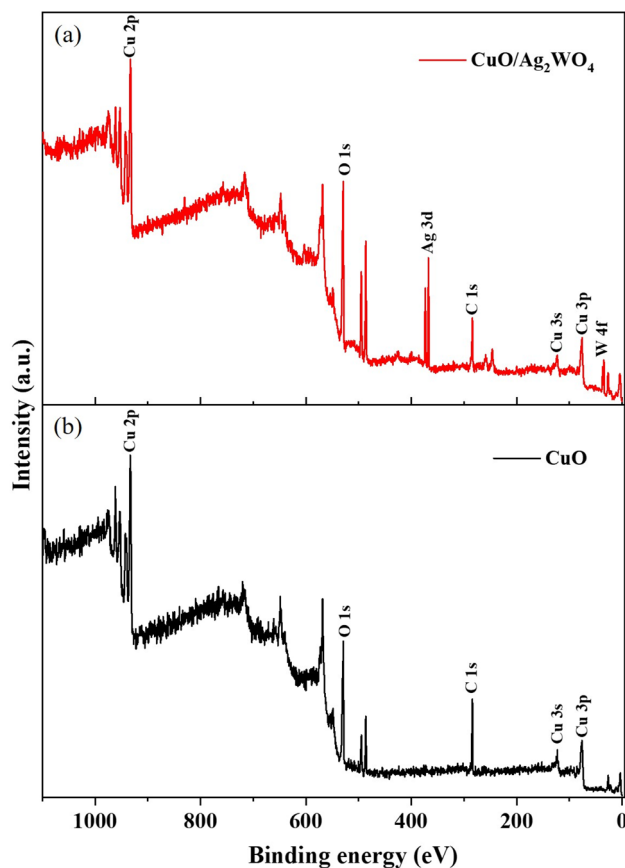
Fig. 6 Wide scan XPS spectrum of pristine CuO NLs and CuO/Ag$_2$WO$_4$ composites, (a) and (b), respectively.

(953.55 eV) due to two natural metallic oxidation states of Cu(I) and Cu(II). Moreover, the appearance of two satellite shake up peaks at 940.80 and 962.20 eV demonstrate the typical features of CuO.[52,53] The deconvolution of high-resolution O 1s spectrum is shown in Fig. 7(b). The high binding region at 532.10 eV can be ascribed to the adsorbed oxygen/water species when sample is exposed to ambient condition, and the other two peaks, one for typical metal–oxygen binding energy at 529.65 eV and second is related to surface defects especially oxygen vacancies at 530.94 eV were well pronounced. Fig. 7(c) illustrates the analysis of high-resolution Ag 3d spectrum. The two peaks can be assigned to Ag 3d$_{5/2}$ (368.05 eV) and Ag 3d$_{3/2}$ (373.90 eV) with spin–orbit splitting difference of 6 eV, indicating the presence of Ag (0) and Ag(I) oxidation states. Furthermore, the Ag 3d spectrum can be deconvoluted into two sets of peaks based on different oxidation states. The feature (blue curve) at the lower binding energies of 367.69 and 373.70 eV can be assigned to Ag$^+$ in Ag$_2$WO$_4$, whereas the one (red curve) at the higher binding energy at 368.22 and 374.25 eV can be assigned to metallic Ag^0. The high-resolution W 4f spectrum is shown in Fig. 7(d). The two peaks could be associated to W 4f$_{7/2}$ (34.90 eV) and W 4f$_{5/2}$ (37.00 eV).[54,55] In this sense, the XPS results confirmed the XRD and EDX results that CuO/Ag$_2$WO$_4$ composites had successfully been formed.

3.2. Photoelectrochemical analysis of CuO/Ag$_2$WO$_4$ composite

PEC studies have been performed on both pure CuO and various CuO/Ag$_2$WO$_4$ composites in 1.0 M NaOH as an aqueous electrolytic solution. Fig. 8(a) displays the photocurrent density *versus* time under both solar radiation illumination and under dark conditions at a voltage of −0.55 V (*vs.* Ag/AgCl) using pristine CuO and two different CuO/Ag$_2$WO$_4$ composites prepared by 5 and 10 SILAR cycles labelled as CuO/Ag$_2$WO$_4$-5 and CuO/Ag$_2$WO$_4$-10, respectively. The photocurrent densities of different materials including original CuO NLs, CuO/Ag$_2$WO$_4$-10, and CuO/Ag$_2$WO$_4$-5, were observed as −0.3, −0.7, and −1.1 mA cm^{-2}, respectively under solar radiation illumination and −0.09, −0.15, and −0.20 mA cm^{-2}, respectively under dark conditions. It is obvious from the photocurrent density that pristine CuO is associated with low current density owing to its low density of active sites and fast charge recombination rate of electron–hole pairs during the illumination of solar light. Hence, we used the SILAR method for the improvement in the photocurrent density of CuO photocathode by depositing Ag$_2$WO$_4$ nanoparticles as co-catalyst. The photocurrent density of CuO/Ag$_2$WO$_4$-5 composite is almost fourfold higher as compared to original CuO NLs, suggesting improved photoactivity of the composite material. Furthermore, optimization was carried out in order to provide a clear picture of the composite system using 10 SILAR cycles of deposition of silver tungstate. The generation of photocurrent density was decreased from −1.1 mA cm^{-2} to −0.7 mA cm^{-2}. Observations of poor performance during a higher number of 10 cycles may be attributed to the high density of Ag$_2$WO$_4$ onto the surface of CuO NLs. This diminishes the charge separation at the interface of the two materials, resulting in poor performance. Additionally, the 10 cycle cannot allow the high density interaction of light photons with the surface of CuO. This interaction could reach its saturation limit, which leads to the relatively low performance of this cycle. Due to their low electrical conductivity, 10 cycles of Ag$_2$WO$_4$ deposition decreased electron transfer and had a negative effect on PEC water splitting. PEC water splitting performance has been reported to be affected by the poor electrical conductivity of thick layer deposited films of different materials.[56] From Fig. 8(a), the photocurrent response in cycle 10 is decreased in comparison to cycle 5. Although the difference in photocurrent between cycles 5 and 10 is not high, if we use cycles 11 and onward, then the photocurrent may be low, as observed in cycle 10. It is obvious from the difference in photocurrent between cycles 5 and 10 that the difference between cycles 6, 7, 8, and 9 could be even lower, therefore we did not study these cycles in this work. Based on the SEM images of CuO nanoleaves on the surfaces of CuO nanoleaves, it can be seen that the deposition of Ag$_2$WO$_4$ material is extremely low for cycles below 5. Therefore, the results indicate that such cycles as 1, 2, 3, and 4 would not produce hydrogen as effectively as cycle 5, therefore we did not report cycles such as 1, 2, 3, and 4. Photoelectrodes were subjected to a two-hour photo-corrosion test under illumination of the solar light (Fig. 8(b)). The initial photocurrent density of the pure CuO photocathode
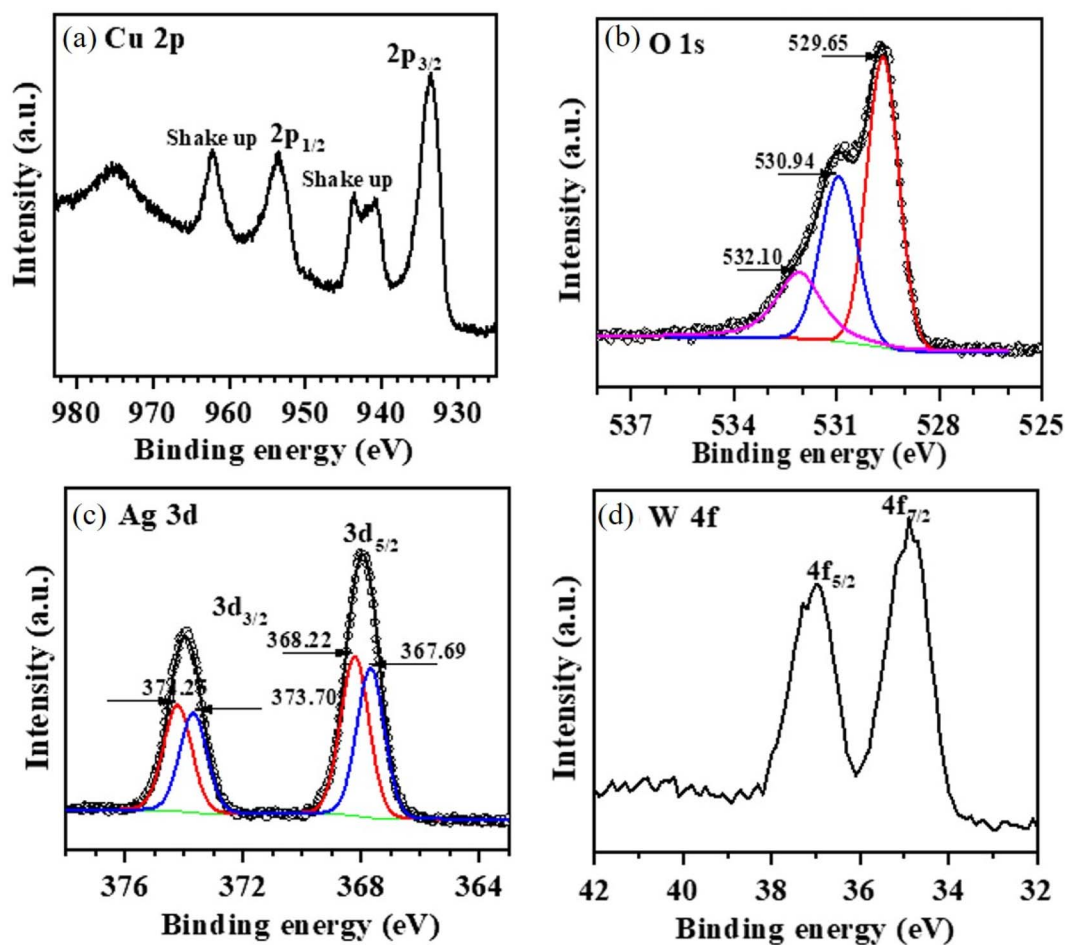
Fig. 7 A high-resolution XPS spectrum for (a) Cu 2p spectrum, (b) O 1s spectrum, (c) Ag 3d spectrum, and (d) W 4f spectrum collected from the CuO/Ag$_2$WO$_4$ composites.

increases from -0.27 to -0.67 mA cm^{-2} within 279 seconds, but then it starts to decline and reaches -0.12 mA cm^{-2}. On the other hand, the photocurrent density of the CuO/Ag$_2$WO$_4$ photocathode increases from -0.80 to -1.12 mA cm^{-2} during the first 194 seconds and then begins to decrease until it reaches -0.24 mA cm^{-2}. It can be concluded from the stability observations that the CuO/Ag$_2$WO$_4$ composite generates a higher current density and is faster than pure CuO. Charge transfer between Ag$_2$WO$_4$ nanoparticles and CuO nanostructures is greatly facilitated by Ag$_2$WO$_4$ nanoparticles on CuO nanostructures. In this way, the uniform distribution of chemical elements in the hybrid system has enabled Ag$_2$WO$_4$ to stabilize CuO NLs in terms of charge transfer. XPS, STEM, and EDX studies have verified this conclusion. In terms of photocurrent density loss, the composite system appears to be relatively stable. In addition to stabilizing CuO, silver tungstate also improves hydrogen production performance. Furthermore, Ag$_2$WO$_4$ nanoparticles contribute to the increased stability of CuO/Ag$_2$WO$_4$-5 in part because they ensure low physical contact between CuO and the electrolyte, and they facilitate the generation of photogenerated electrons by the co-catalyst.

Using chronoamperometric response, the photocatalytic stability of CuO/Ag$_2$WO$_4$-5 was also evaluated under a fixed

negative potential of -0.55 V (Fig. 8(b)). This graph illustrates the variation in the photocurrent density of CuO and CuO/Ag$_2$WO$_4$-5 hybrid materials over time. The use of the -0.55 V fixed negative potential can produce the large HER current and it avoids the electroreduction of copper ions and silver ions into their metallic atoms because their reduction potentials are even larger than the fixed negative potential of -0.55 V. Because we did not see the possibility of reducing these metallic ions, we maintained the stability of the hybrid system for an extended period of time. As compared to pristine CuO, hybrid CuO/Ag$_2$WO$_4$-5 material exhibits the largest photocurrent when a fixed negative potential of -0.55 V is applied, which confirms the suitability of hybrid systems for the production of hydrogen in practical applications. A linear sweep voltammetry (LSV) measurement was conducted in the presence of a normal supply of room light. Fig. 8(c) shows significant improvements in CuO/Ag$_2$WO$_4$ photoelectrode photocurrent density associated with the heterojunction effect associated with the deposition of Ag$_2$WO$_4$ nanoparticles onto CuO NLs surfaces. As a result, a large number of electrons generated by the photoelectrode are readily transferred to the counter electrode *via* the external circuit, resulting in a higher photocurrent density. Increasing the separation of charge carriers and transport
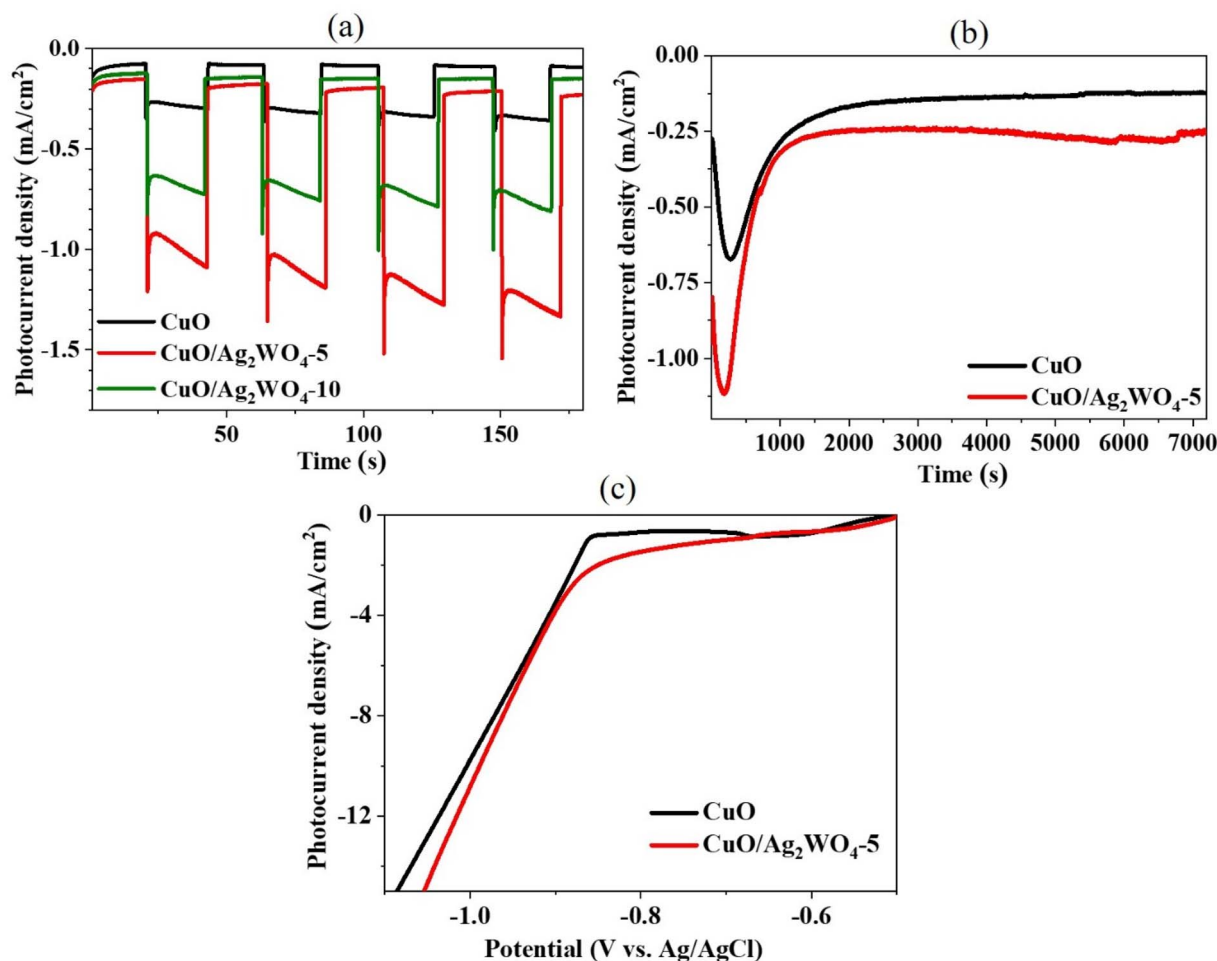
Fig. 8 (a) The responses of CuO, CuO/Ag$_2$WO$_4$-5, and CuO/Ag$_2$WO$_4$-10 photoelectrodes to solar illumination and under ambient dark conditions, (b) the response of CuO and CuO/Ag$_2$WO$_4$-5 photoelectrodes for 2 hours under illumination, and (c) LSV curves under normal room light of the CuO and CuO/Ag$_2$WO$_4$-5 photoelectrodes.

efficiency, absorbing solar light at an increased rate, and increasing the absorption of visible wavelengths are the reasons for this.

In order to find the flat-band potential V_{fb} and free carrier concentration N_A of photoelectrodes, a Mott–Schottky (M–S) measurement was used with the following relationship:[57]

$$\frac{1}{C^2} = \frac{2}{\varepsilon_r \varepsilon_0 e N_A} \left(V - V_{fb} - \frac{kT}{e} \right)$$

where C is the capacitance of the space charge layer, ε_r the relative permittivity of the semiconductor, ε_0 permittivity of free space, e the elementary charge of an electron, V the applied potential, k Boltzmann constant, and T is the temperature.

Fig. 9(a) shows the (M–S) plots for pristine CuO and the CuO/Ag$_2$WO$_4$-5 photoelectrodes. It is clear that both slopes of CuO and the CuO/Ag$_2$WO$_4$-5 photoelectrodes are negative which indicate that both materials are photocathodes (p-type semiconductors) and the space charge is populated with electrons. The flat-band potentials for pristine CuO and CuO/Ag$_2$WO$_4$-5 photocathodes are approximately equal to 0.38 and 0.14 V, respectively, while the free carrier concentration (the acceptor

concentration in these cases) for pristine CuO and CuO/Ag$_2$WO$_4$-5 samples were estimated to be 6.9×10^{20} and 6.6×10^{21} cm^{-3} respectively. According to these findings, the deposition of the Ag$_2$WO$_4$ nanoparticles onto the CuO NLs increases the electron transfer between the photocathode and the electrolyte and lowers the redox potential at the CuO/Ag$_2$WO$_4$-5 surface, which results in high photoactivity towards the hydrogen evolution reaction (HER).

Charge transport phenomena were quantified using electrochemical impedance spectroscopy (EIS) to understand the reaction kinetics of HER. As shown in Fig. 9(b), the Nyquist plots for pristine CuO and pristine CuO/Ag$_2$WO$_4$-5 electrodes are presented. Nyquist plots with high frequencies have semicircles, while those with low frequencies have straight tails. It is generally understood that the radius of the arc indicates the magnitude of the charge-transfer resistance (R_{ct}), while the straight tail indicates the effect of the charge diffusion procedure on the Warburg impedance (Z_W) of the electrode. Using Randles–Ershler equivalent circuits to fit Nyquist plots, Fig. 9(b) illustrates such circuits.[58,59]
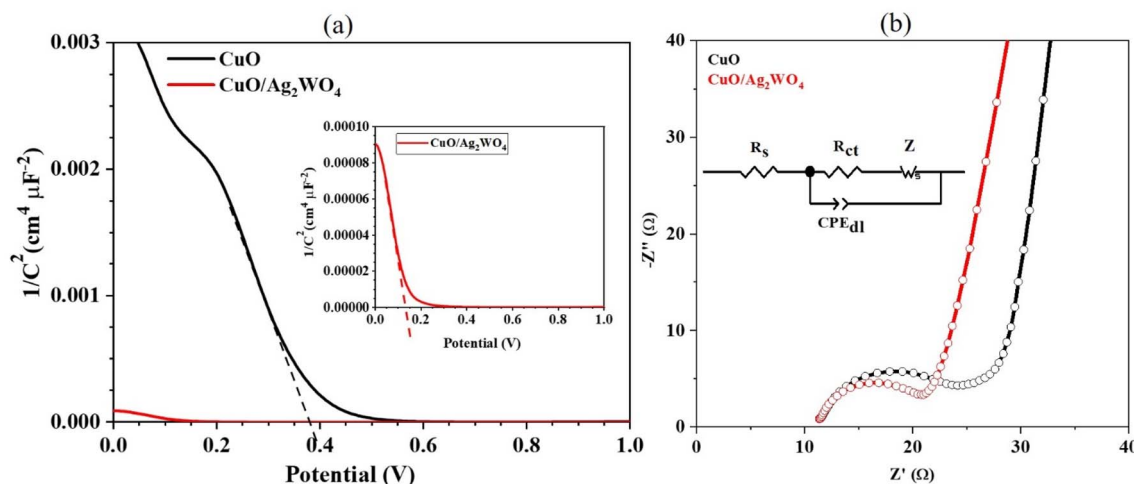
Fig. 9 (a) The M–S plots of CuO and CuO/Ag$_2$W$_4$ photoelectrodes and (b) the EIS spectra acquired on CuO and CuO/Ag$_2$WO$_4$ photoelectrodes with equivalent circuits.

It is interesting to note that the CuO/Ag$_2$WO$_4$-5 photo-electrode in Fig. 9(b) demonstrated a significantly smaller charge transfer resistance (13.77 Ω) compared to the pristine CuO photoelectrode (18.35 Ω). A lower charge transfer resistance for the CuO/Ag$_2$WO$_4$ composite with 5 cycles enabled fast kinetics during the HER process. Moreover, the capacitance double layer for pure CuO and CuO/Ag$_2$WO$_4$-5 photoelectrode were as 0.03 and 0.01 from the EIS fitted data.

In order to estimate the electrochemical potential surface area (ECSA), cyclic voltammetry (CV) was utilized at different scan rates as shown in (Fig. 10(a–d)). According to existing literature,[60] CV curves at different scan rates were used to calculate the ECSA in non-faradic regions; thus, studies under non-faradic regions for the calculation of ECSA have been published. The non-faradic region of CV curves actually depicts the number of active sites present on the electrode surface that participate in electrochemical reactions. From the slope of the linear fit of the average current density *versus* the scan rate, we determined the ECSA of pure CuO (1.6×10^{-5} F cm^{-2}) and CuO/Ag$_2$WO$_4$-5 (2.8×10^{-5} F cm^{-2}). Composite catalysts have shown

a high number of active sites and significantly sped up the CuO/Ag$_2$WO$_4$-5-based HER process. By developing an optimal inter-face for the acceleration of charge transport and minimizing physical contact between the CuO photocathode and electrolyte, the CuO/Ag$_2$WO$_4$-5 composite system achieved enhanced water splitting performance. Additionally, the architecture of the CuO NLs, tuned surface of the composite system after deposition of Ag$_2$WO$_4$ nanoparticles as co-catalysts, high density of active sites, and fast charge transfer rate are all factors contributing to the improved performance.

3.3. Photoelectrochemical HER mechanism on CuO/Ag$_2$WO$_4$ composite

The enhanced PEC photo-reactivity is likely caused by electron and hole separation and transfer at the photoelectrode inter-faces. Electrons and holes were generated and separated much more easily in CuO/Ag$_2$WO$_4$-5 composites due to drastic differences in band edge potentials. A semiconductor's edge potential can be estimated using the Mulliken electronegativity
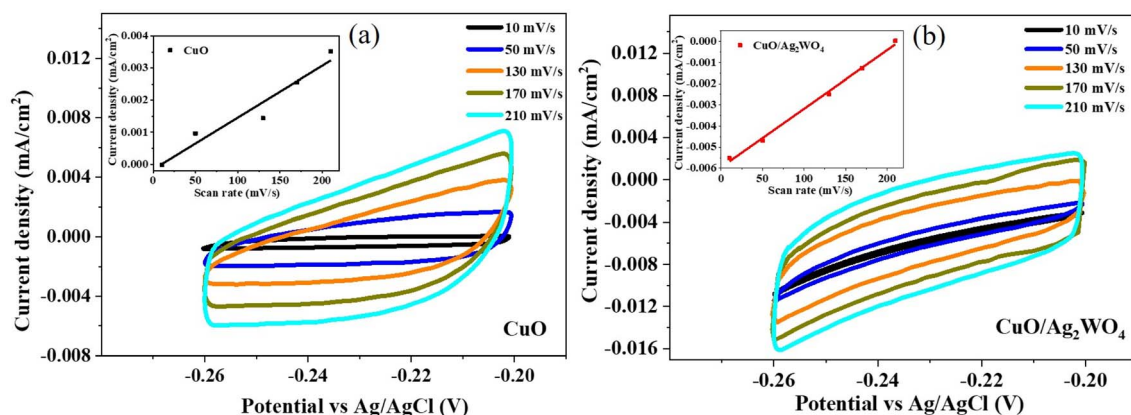

Fig. 10 A cyclic voltammetry analysis of electrochemical active surface area and a linear fit for (a) CuO and (b) CuO/Ag$_2$WO$_4$ photoelectrodes.
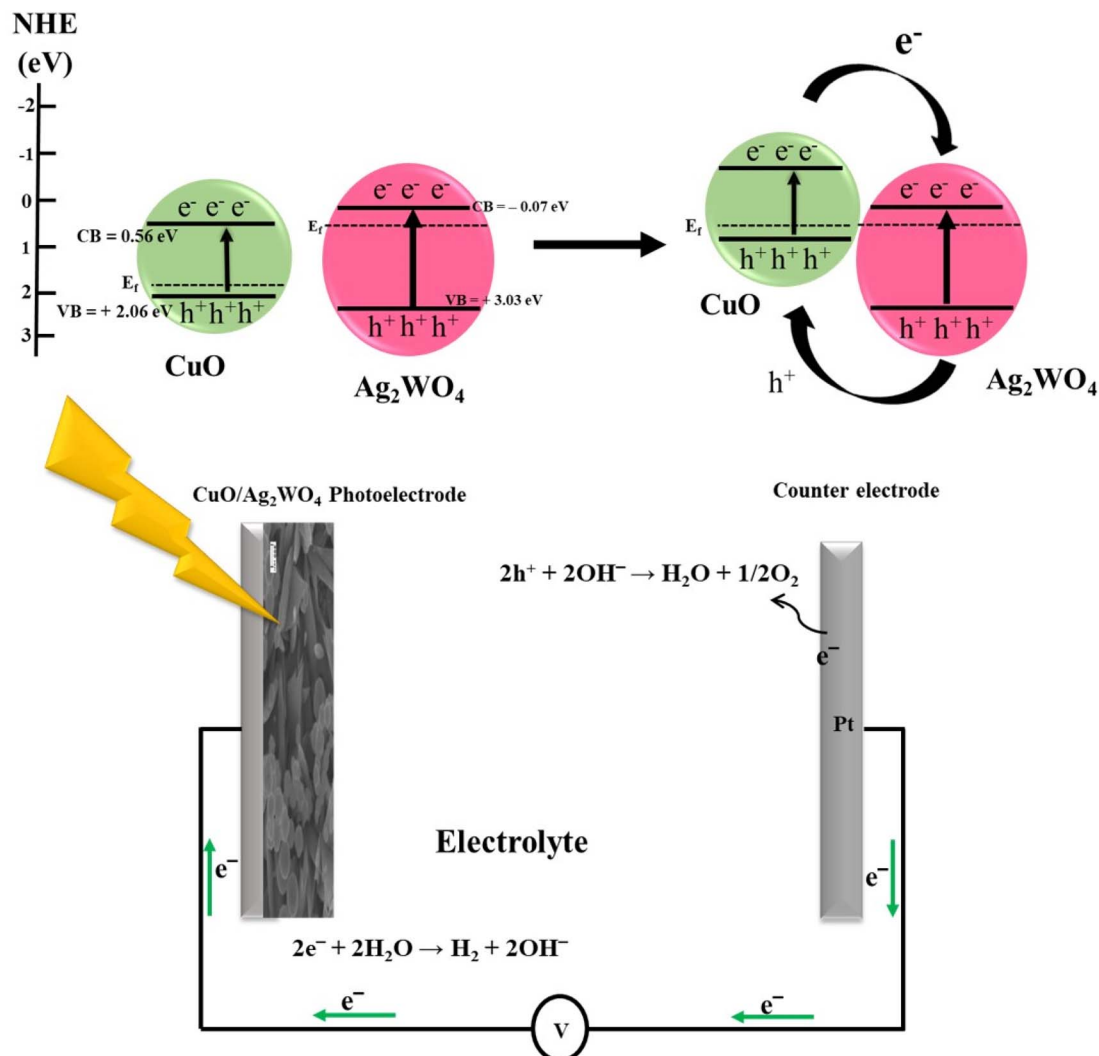
Fig. 11 An analysis of the possible mechanisms of the CuO/Ag₂WO₄ photoelectrode with band edge potentials.

theory[44] in the valence band (VB) and in the conduction band (CB) at zero charge:

$$E_{VB} = X - E^e + 0.5E_g \quad (1)$$

There are four parameters in this equation, whereas E_{VB} the VB edge potential, X is the absolute electronegativity of the semiconductor, E^e is the free electron energy on a hydrogen scale, 4.5 eV, and E_g is the band gap energy of the semiconductor. Using the following formula, the edge potential of the CB (E_{CB}) can be calculated:

$$E_{CB} = E_{VB} - E_g \quad (2)$$

As a result of this equation, CuO has an X value of 5.81 eV and Ag₂WO₄ has an X value of 5.98 eV, and the band gaps are 1.5 and 3.1 eV, respectively.[44,61–63] As a result, pristine CuO and Ag₂WO₄ have the same E_{VBs}, which are +2.06 eV and +3.03 eV, respectively. CuO and Ag₂WO₄ also show similar E_{CB} values, both at +0.56 eV. As shown in Fig. 11, a possible mechanism underpinning PEC activity is outlined.

A CuO/Ag₂WO₄-5 composite is formed when CuO nanoleaves are embedded in Ag₂WO₄ nanoparticles, resulting in the Fermi levels aligning to achieve equilibrium.[42] Fermi levels of CuO and Ag₂WO₄ coexist simultaneously because CuO has a greater Fermi potential than Ag₂WO₄; electrons in the Fermi levels of CuO and Ag₂WO₄ move toward one another until they reach equilibrium.

In the VB, light vibrates photons, which excited electrons to a higher potential. In CuO and Ag₂WO₄, electrons were excited to a potential of +0.56 eV and −0.07 eV, respectively. The photo-generated electrons generated by CuO produced by the CB of Ag₂WO₄ can move effectively to the photocathode and contribute to HER. Nanoparticles would transfer holes from their valence bands to the electrode and thus, enhance efficiency at the electrode–electrolyte interface. By limiting electron/hole recombination, this transfer enhances the efficiency of charge carrier separation while reducing electron/hole recombination. Photo-generated charge carriers are separated and transferred by this mechanism, improving the efficiency of PEC water splitting.

4 Conclusions

To summarize, we have synthesized an improved CuO/Ag_2WO_4-5 photocathode that is effective for PEC water splitting when illuminated by solar light. Samples were grown using the hydrothermal method followed by the SILAR method. FE-SEM, XRD, EDX, and XPS techniques are used to characterize the synthesized materials. CuO/Ag_2WO_4-5 photocathode demonstrated efficient PEC water splitting in comparison to CuO/Ag_2WO_4-10 photocathode and pristine CuO photocathode in alkaline media. As an alternative composite photocathode material suitable for solar-driven hydrogen production, CuO/Ag_2WO_4-5 composites are recommended for their low overpotential, stability, and photocurrent density. A facile, low-cost, low-emission approach to the preparation of composite materials is highly advantageous in terms of societal needs and technological advancement.

Abbreviations

CuO	Cupric oxide
Ag_2WO_4	Silver tungstate
PEC	Photoelectrochemical
NRs	Nanorods
SILAR	Successive ionic layer adsorption and reaction
XRD	X-Ray diffraction
FE-SEM	Field-emission scanning electron microscope
EDX	Energy-dispersive X-ray
HAADF-STEM	High-angle annular dark-field – scanning transmission electron microscope
XPS	X-Ray photoelectron spectroscopy
LSV	Linear sweep voltammetry
M–S	Mott–Schottky

Author contributions

Elfatih Mustafa (E. M.); writing original draft, conceptualization, prepared, characterized all samples, analyzed the data, E. A. Dawi (E. D.); writing original draft, conceptualization, investigations, Z. H. Ibupoto (Z. I.); conceptualization, writing original draft, sample analysis, A. M. M. Ibrahim (A. I.), revised draft, investigations, experimental analysis, A. Elsukova (A. E.); investigations, measurements, revised manuscript, X. Liu (X. L.); investigations, experimental analysis, sources, Aneela Tahira (A. T.); experimental analysis, sources, revised final draft, R. E. Adam (R. A.); conceptualization, investigation, sources, M. Willander (M. W.); conceptualization, writing original draft, supervision, O. Nur (O. N.); conceptualization, investigation, sources, revised final draft.

Conflicts of interest

Authors declare no conflicts of interest.

Acknowledgements

References

1 H. B. Gray, Powering the planet with solar fuel, *Nat. Chem.*, 2009, **1**, 7, DOI: **10.1038/nchem.141**.

2 I. Dincer and C. Acar, Review and evaluation of hydrogen production methods for better sustainability, *Int. J. Hydrogen Energy.*, 2015, **40**, 11094–11111, DOI: **10.1016/j.ijhydene.2014.12.035**.

3 S. Y. Tee, K. Y. Win, W. S. Teo, L.-D. Koh, S. Liu, C. P. Teng and M.-Y. Han, Recent Progress in Energy-Driven Water Splitting, *Adv. Sci.*, 2017, **4**, 1600337, DOI: **10.1002/advs.201600337**.

4 J. A. Turner, Sustainable Hydrogen Production, *Science*, 2004, **305**, 972–974, DOI: **10.1126/science.1103197**.

5 A. Kudo and Y. Miseki, Heterogeneous photocatalyst materials for water splitting, *Chem. Soc. Rev.*, 2009, **38**, 253–278, DOI: **10.1039/b800489g**.

6 M. G. Walter, E. L. Warren, J. R. McKone, S. W. Boettcher, Q. Mi, E. A. Santori and N. S. Lewis, Solar water splitting cells, *Chem. Rev.*, 2010, **110**, 6446–6473, DOI: **10.1021/cr1002326**.

7 A. Fujishima and K. Honda, Electrochemical Photolysis of Water at a Semiconductor Electrode, *Nature*, 1972, **238**, 37–38, DOI: **10.1038/238037a0**.

8 W. Yang, R. R. Prabhakar, J. Tan, S. D. Tilley and J. Moon, Strategies for enhancing the photocurrent, photovoltage, and stability of photoelectrodes for photoelectrochemical water splitting, *Chem. Soc. Rev.*, 2019, **48**, 4979–5015, DOI: **10.1039/c8cs00997j**.

9 J. W. Ager, M. R. Shaner, K. A. Walczak, I. D. Sharp and S. Ardo, Experimental demonstrations of spontaneous, solar-driven photoelectrochemical water splitting, *Energy Environ. Sci.*, 2015, **8**, 2811–2824, DOI: **10.1039/c5ee00457h**.

10 K. T. Fountaine, H. J. Lewerenz and H. A. Atwater, Efficiency limits for photoelectrochemical water-splitting, *Nat. Commun.*, 2016, **7**, 1–9, DOI: **10.1038/ncomms13706**.

11 Y. Yang, D. Xu, Q. Wu and P. Diao, Cu_2O/CuO bilayered composite as a high-efficiency photocathode for photoelectrochemical hydrogen evolution reaction, *Sci. Rep.*, 2016, **6**, 35158, DOI: **10.1038/srep35158**.

12 A. L. Linsebigler, G. Lu and J. T. Yates, Photocatalysis on TiO_2 Surfaces: Principles, Mechanisms, and Selected Results, *Chem. Rev.*, 1995, **95**, 735–758, DOI: **10.1021/cr00035a013**.

13 W. Li, P. Da, Y. Zhang, Y. Wang, X. Lin, X. Gong and G. Zheng, WO3 Nanoflakes for Enhanced Photoelectrochemical Conversion, *ACS Nano*, 2014, **8**, 11770–11777, DOI: **10.1021/nn5053684**.

14 Z. Kang, H. Si, S. Zhang, J. Wu, Y. Sun, Q. Liao, Z. Zhang and Y. Zhang, Interface Engineering for Modulation of Charge Carrier Behavior in ZnO Photoelectrochemical Water Splitting, *Adv. Funct. Mater.*, 2019, **29**, 1–19, DOI: **10.1002/adfm.201808032**.

15 K. Sivula, F. Le Formal and M. Grätzel, Solar water splitting: Progress using hematite (α-Fe_2O_3) photoelectrodes, *ChemSusChem*, 2011, **4**, 432–449, DOI: **10.1002/cssc.201000416**.

16 T. W. Kim and K.-S. Choi, Nanoporous $BiVO_4$ Photoanodes with Dual-Layer Oxygen Evolution Catalysts for Solar Water Splitting, *Science*, 2014, **343**, 990–994, DOI: **10.1126/science.1246913**.

17 Z. Chen, Y. Li, L. Wang, Y. Bu and J. P. Ao, Development of a bi-compound heterogeneous cocatalyst modified p-Si photocathode for boosting the photoelectrochemical water splitting performance, *J. Mater. Chem. A*, 2021, **9**, 9157–9164, DOI: **10.1039/d0ta12161d**.

18 D. Chen, Z. Liu, Z. Guo, W. Yan and Y. Xin, Enhancing light harvesting and charge separation of Cu_2O photocathodes with spatially separated noble-metal cocatalysts towards highly efficient water splitting, *J. Mater. Chem. A*, 2018, **6**, 20393–20401, DOI: **10.1039/c8ta07503d**.

19 H. Xing, E. Lei, Z. Guo, D. Zhao, X. Li and Z. Liu, Exposing the photocorrosion mechanism and control strategies of a CuO photocathode, *Inorg. Chem. Front.*, 2019, **6**, 2488–2499, DOI: **10.1039/c9qi00780f**.

20 N. Kornienko, N. A. Gibson, H. Zhang, S. W. Eaton, Y. Yu, S. Aloni, S. R. Leone and P. Yang, Growth and Photoelectrochemical Energy Conversion of Wurtzite Indium Phosphide Nanowire Arrays, *ACS Nano*, 2016, **10**, 5525–5535, DOI: **10.1021/acsnano.6b02083**.

21 Q. Huang, Q. Li and X. Xiao, Hydrogen evolution from Pt nanoparticles covered p-type CdS:Cu photocathode in scavenger-free electrolyte, *J. Phys. Chem. C.*, 2014, **118**, 2306–2311, DOI: **10.1021/jp410242e**.

22 S. Ida, K. Yamada, T. Matsunaga, H. Hagiwara, Y. Matsumoto and T. Ishihara, Preparation of p-type $CaFe_2O_4$ photocathodes for producing hydrogen from water, *J. Am. Chem. Soc.*, 2010, **132**, 17343–17345, DOI: **10.1021/ja106930f**.

23 Y. J. Jang and J. S. Lee, Photoelectrochemical Water Splitting with p-Type Metal Oxide Semiconductor Photocathodes, *ChemSusChem*, 2019, **12**, 1835–1845, DOI: **10.1002/cssc.201802596**.

24 A. Cots, P. Bonete and R. Gómez, Improving the Stability and Efficiency of CuO Photocathodes for Solar Hydrogen Production through Modification with Iron, *ACS Appl. Mater. Interfaces*, 2018, **10**, 26348–26356, DOI: **10.1021/acsami.8b09892**.

25 X. Xiong, C. You, Z. Liu, A. M. Asiri and X. Sun, Co-Doped CuO Nanoarray: An Efficient Oxygen Evolution Reaction Electrocatalyst with Enhanced Activity, *ACS Sustainable Chem. Eng.*, 2018, **6**, 2883–2887, DOI: **10.1021/acssuschemeng.7b03752**.

26 Q. Zhou, T. T. Li, J. Qian, W. Xu, Y. Hu and Y. Q. Zheng, CuO Nanorod Arrays Shelled with Amorphous NiFe Layered Double Hydroxide Film for Enhanced Electrocatalytic Water Oxidation Activity, *ACS Appl. Energy Mater.*, 2018, **1**, 1364–1373, DOI: **10.1021/acsaem.8b00076**.

27 P. K. Samal, L. Sharma and A. Halder, Enhanced photoelectrochemical hydrogen evolution by 2D nanoleaf structured CuO, *J. Appl. Phys.*, 2020, **127**, 194902, DOI: **10.1063/1.5140207**.

28 W. Septina, R. R. Prabhakar, R. Wick, T. Moehl and S. D. Tilley, Stabilized Solar Hydrogen Production with CuO/CdS Heterojunction Thin Film Photocathodes, *Chem. Mater.*, 2017, **29**, 1735–1743, DOI: **10.1021/acs.chemmater.6b05248**.

29 Y. S. Kim, I. S. Hwang, S. J. Kim, C. Y. Lee and J. H. Lee, CuO nanowire gas sensors for air quality control in automotive cabin, *Sens. Actuators, B*, 2008, **135**, 298–303, DOI: **10.1016/j.snb.2008.08.026**.

30 J. Liu, J. Jin, Z. Deng, S. Z. Huang, Z. Y. Hu, L. Wang, C. Wang, L. H. Chen, Y. Li, G. Van Tendeloo and B. L. Su, Tailoring CuO nanostructures for enhanced photocatalytic property, *J. Colloid Interface Sci.*, 2012, **384**, 1–9, DOI: **10.1016/j.jcis.2012.06.044**.

31 A. Banerjee, U. Singh, V. Aravindan, M. Srinivasan and S. Ogale, Synthesis of CuO nanostructures from Cu-based metal organic framework (MOF-199) for application as anode for Li-ion batteries, *Nano Energy*, 2013, **2**, 1158–1163, DOI: **10.1016/j.nanoen.2013.04.008**.

32 H. Kidowaki, T. Oku, T. Akiyama, A. Suzuki, B. Jeyadevan and J. Cuya, Fabrication and Characterization of CuO-based Solar Cells, *J. Mater. Sci. Res.*, 2011, **1**, 138–143, DOI: **10.5539/jmsr.v1n1p138**.

33 S. Masudy-Panah, R. Siavash Moakhar, C. S. Chua, H. R. Tan, T. I. Wong, D. Chi and G. K. Dalapati, Nanocrystal Engineering of Sputter-Grown CuO Photocathode for Visible-Light-Driven Electrochemical Water Splitting, *ACS Appl. Mater. Interfaces*, 2016, **8**, 1206–1213, DOI: **10.1021/acsami.5b09613**.

34 S. Won Hwang, G. Sang Han, J. Young Cho, D. Un Lee, H. Soo Han and I. Sun Cho, Sharp-edged Nanoflakes Array of CuO with Enhanced Optical and Charge Transport Properties for Bias-Free Tandem Solar Water-splitting, *Appl. Surf. Sci.*, 2022, **585**, 152632, DOI: **10.1016/j.apsusc.2022.152632**.

35 F. P. Koffyberg and F. A. Benko, A photoelectrochemical determination of the position of the conduction and valence band edges of p-type CuO, *J. Appl. Phys.*, 1982, **53**, 1173–1177, DOI: **10.1063/1.330567**.

36 M. Einert, T. Weller, T. Leichtweiß, B. M. Smarsly and R. Marschall, Electrospun CuO Nanofibers: Stable Nanostructures for Solar Water Splitting, *ChemPhotoChem*, 2017, **1**, 326–340, DOI: **10.1002/cptc.201700050**.

37 S. John, S. S. Vadla and S. C. Roy, High photoelectrochemical activity of CuO nanoflakes grown on Cu foil, *Electrochim. Acta.*, 2019, **319**, 390–399, DOI: **10.1016/j.electacta.2019.07.008**.

38 V. Ragupathi, M. A. Raja, P. Panigrahi and N. Ganapathi Subramaniam, CuO/g-C_3N_4 nanocomposite as promising photocatalyst for photoelectrochemical water splitting,

Optik (Stuttg), 2020, **208**, 164569, DOI: **10.1016/j.ijleo.2020.164569**.

39 H. L. S. Santos, P. G. Corradini, M. A. S. Andrade and L. H. Mascaro, CuO/NiOx thin film–based photocathodes for photoelectrochemical water splitting, *J. Solid State Electrochem.*, 2020, **24**, 1899–1908, DOI: **10.1007/s10008-020-04513-5**.

40 Q. Zhang, K. Zhang, D. Xu, G. Yang, H. Huang, F. Nie, C. Liu and S. Yang, CuO nanostructures: synthesis, characterization, growth mechanisms, fundamental properties, and applications, *Prog. Mater. Sci.*, 2014, **60**, 208–337, DOI: **10.1016/j.pmatsci.2013.09.003**.

41 J. Li, W. Fang, C. Yu, W. Zhou, L. Zhu and Y. Xie, Ag-based semiconductor photocatalysts in environmental purification, *Appl. Surf. Sci.*, 2015, **358**, 46–56, DOI: **10.1016/j.apsusc.2015.07.139**.

42 M. Pirhashemi, S. Elhag, R. E. Adam, A. Habibi-Yangjeh, X. Liu, M. Willander and O. Nur, n–n ZnO–Ag$_2$CrO$_4$ heterojunction photoelectrodes with enhanced visible-light photoelectrochemical properties, *RSC Adv*, 2019, **9**, 7992–8001, DOI: **10.1039/c9ra00639g**.

43 S. Zhang, Z. Liu, Y. Zhang, S. Gao, R. Jin and Q. Wang, Highly effective photoelectrochemical performance of solar energy materials based on Ag$_2$WO$_4$–AgX (X = Cl, Br, I) sensitized TiO$_2$ nanotube arrays, *Ceram. Int.*, 2018, **44**, 6659–6665, DOI: **10.1016/j.ceramint.2018.01.077**.

44 R. E. Adam, M. Pirhashemi, S. Elhag, X. Liu, A. Habibi-Yangjeh, M. Willander and O. Nur, ZnO/Ag/Ag$_2$WO$_4$ photo-electrodes with plasmonic behavior for enhanced photoelectrochemical water oxidation, *RSC Adv*, 2019, **9**, 8271–8279, DOI: **10.1039/c8ra10141h**.

45 S. Feizpoor and A. Habibi-Yangjeh, Integration of Ag$_2$WO$_4$ and AgBr with TiO$_2$ to fabricate ternary nanocomposites: Novel plasmonic photocatalysts with remarkable activity under visible light, *Mater. Res. Bull.*, 2018, **99**, 93–102, DOI: **10.1016/j.materresbull.2017.10.028**.

46 D. Gao, S. Zheng, L. Wang, C. Wang, H. Zhang and Q. Wang, SILAR preparation of visible-light-driven TiO$_2$ NTs/Ag$_2$WO$_4$-AgI photoelectrodes for waste water treatment and photoelectric conversion, *Sep. Purif. Technol.*, 2019, **224**, 308–314, DOI: **10.1016/j.seppur.2019.05.050**.

47 E. Mustafa, R. E. Adam, P. Rouf, M. Willander and O. Nur, Solar-Driven Photoelectrochemical Performance of Novel ZnO/Ag$_2$WO$_4$/AgBr Nanorods-Based Photoelectrodes, *Nanoscale Res. Lett.*, 2021, **16**, 133, DOI: **10.1186/s11671-021-03586-z**.

48 S. P. Ratnayake, J. Ren, E. Colusso, M. Guglielmi, A. Martucci and E. Della Gaspera, SILAR Deposition of Metal Oxide Nanostructured Films, *Small*, 2021, **17**, 2101666, DOI: **10.1002/smll.202101666**.

49 A. Monshi, M. R. Foroughi and M. R. Monshi, Modified Scherrer Equation to Estimate More Accurately Nano-Crystallite Size Using XRD, *World J. Nano Sci. Eng.*, 2012, **02**, 154–160, DOI: **10.4236/wjnse.2012.23020**.

50 T. T. Lun, C. Q. Liu, N. Wang, X. N. Zhai, M. S. Song, Q. Ge, X. Y. Zhang, S. M. Liu, H. L. Wang, W. W. Jiang and W. Y. Ding, Preparation of compact CuO films by sol–gel

51 spin coating technique, *Mater. Lett.*, 2019, **257**, 126745, DOI: **10.1016/j.matlet.2019.126745**.

51 S. Senobari and A. Nezamzadeh-Ejhieh, A comprehensive study on the enhanced photocatalytic activity of CuO–NiO nanoparticles: designing the experiments, *J. Mol. Liq.*, 2018, **261**, 208–217, DOI: **10.1016/j.molliq.2018.04.028**.

52 D. Briggs, X-Ray Photoelectron Spectroscopy (XPS), *Handb. Adhes.*, 2nd edn, 2005, pp. 621–622, DOI: **10.1002/0470014229.ch22**.

53 Z. H. Ibupoto, K. Khun, X. Liu and M. Willander, Low temperature synthesis of seed mediated CuO bundle of nanowires, their structural characterisation and cholesterol detection, *Mater. Sci. Eng., C*, 2013, **33**, 3889–3898, DOI: **10.1016/j.msec.2013.05.029**.

54 K. Dai, J. Lv, L. Lu, C. Liang, L. Geng and G. Zhu, A facile fabrication of plasmonic g-C$_3$N$_4$/Ag$_2$WO$_4$/Ag ternary heterojunction visible-light photocatalyst, *Mater. Chem. Phys.*, 2016, **177**, 529–537, DOI: **10.1016/j.matchemphys.2016.04.065**.

55 X. Y. Zhang, J. D. Wang, J. K. Liu, X. H. Yang and Y. Lu, Construction of silver tungstate multilevel sphere clusters by controlling the energy distribution on the crystal surface, *CrystEngComm*, 2015, **17**, 1129–1138, DOI: **10.1039/c4ce02089h**.

56 W. L. Jang, Y. M. Lu, W. S. Hwang and W. C. Chen, Electrical properties of Li-doped NiO films, *J. Eur. Ceram. Soc.*, 2010, **30**, 503–508, DOI: **10.1016/j.jeurceramsoc.2009.05.041**.

57 F. Jamali-Sheini, M. Cheraghizade and R. Yousefi, SnS nanosheet films deposited *via* thermal evaporation: the effects of buffer layers on photovoltaic performance, *Sol. Energy Mater. Sol. Cells.*, 2016, **154**, 49–56, DOI: **10.1016/j.solmat.2016.04.006**.

58 H. Herrera Hernández, F. González Díaz, G. D. J. Fajardo San Miguel, J. C. Velázquez Altamirano, C. O. González Morán and J. Morales Hernández, Electrochemical Impedance Spectroscopy as a Practical Tool for Monitoring the Carbonation Process on Reinforced Concrete Structures, *Arabian J. Sci. Eng.*, 2019, **44**, 10087–10103, DOI: **10.1007/s13369-019-04041-z**.

59 J. Huang, Z. Yang, Z. Feng, X. Xie and X. Wen, A novel ZnO@Ag@polypyrrole hybrid composite evaluated as anode material for zinc-based secondary cell, *Sci. Rep.*, 2016, **6**, 1–12, DOI: **10.1038/srep24471**.

60 Z. H. Ibupoto, A. Tahira, A. A. Shah, U. Aftab, M. Y. Solangi, J. A. Leghari, A. H. Samoon, A. L. Bhatti, M. A. Bhatti, R. Mazzaro, V. Morandi, M. I. Abro, A. Nafady, A. M. Al-Enizi, M. Emo and B. Vigolo, NiCo$_2$O$_4$ nanostructures loaded onto pencil graphite rod: an advanced composite material for oxygen evolution reaction, *Int. J. Hydrogen Energy.*, 2022, **47**, 6650–6665, DOI: **10.1016/j.ijhydene.2021.12.024**.

61 J. Zhang, H. Cui, B. Wang, C. Li, J. Zhai and Q. Li, Preparation and characterization of fly ash cenospheres supported CuO-BiVO$_4$ heterojunction composite, *Appl. Surf. Sci.*, 2014, **300**, 51–57, DOI: **10.1016/j.apsusc.2014.02.001**.

62 H. qing Jiang, H. Endo, H. Natori, M. Nagai and K. Kobayashi, Fabrication and efficient photocatalytic

degradation of methylene blue over CuO/BiVO$_4$ composite under visible-light irradiation, *Mater. Res. Bull.*, 2009, **44**, 700–706, DOI: **10.1016/j.materresbull.2008.06.007**.

63 S. Sharma, M. R. Pai, G. Kaur, Divya, V. R. Satsangi, S. Dass and R. Shrivastav, Efficient hydrogen generation on CuO core/Ag–TiO$_2$ shell nano-hetero-structures by photocatalytic splitting of water, *Renewable Energy*, 2019, **136**, 1202–1216, DOI: **10.1016/j.renene.2018.09.091**.